Numerical approach for the simulation of flow-induced noise around a structure with complex geometry: high-speed train bogie in a cavity

Yuan He[1], David Thompson[1] and Zhiwei Hu[2]

[1]Institute of Sound and Vibration Research, Faculty of Engineering and Physical Sciences, University of Southampton, Southampton, UK.
[2]Aerodynamics and Flight Mechanics Research Group, Faculty of Engineering and Physical Sciences, University of Southampton, Southampton, UK.

Abstract

The bogie region is a significant aerodynamic noise source on high-speed trains. Due to its complex geometry and flow field, numerical simulations using Computational Fluid Dynamics are especially challenging. The main challenge is to achieve a grid with adequate resolution, especially in the boundary layer, while ensuring computational affordability. This study addresses the challenge by employing a hybrid grid, integrating structured hexahedral mesh near solid surfaces with unstructured polyhedral mesh in the remaining volume. To limit the number of cells in the boundary layer region, the Delayed Detached Eddy Simulation method is selected. Additionally, to achieve a further reduction in the cell count, the Reynolds number of the model is decreased by scaling down the model size and lowering the inflow speed. The hybrid grid generation and numerical settings are guided by validated simulations of flow over cylinders. A grid sensitivity study, conducted with a simplified half-width bogie model, reveals the meshing requirements for the full-width model. Aerodynamic results highlight the rear section of the cavity and bogie as primary noise sources, emphasizing the critical role of the detached shear layer from upstream components. Time-resolved surface pressure data are input into the Ffowcs-Williams and Hawkings equation for far-field noise calculation. The results indicate that the sound energy is concentrated below 200 Hz in the full-scale model, with the cavity contributing more than the bogie. This study provides a practical numerical approach for simulating a structure with complex geometry, offering insights for realistic model simulations.

Keywords: Train bogie; aerodynamic noise; simplified cavity; hybrid grid; DDES; Ffowcs-Williams and Hawkings

1. Introduction

The significance of aerodynamic noise from high-speed trains intensifies with increasing train speeds. Aerodynamic noise, which includes contributions from car body surfaces, inter-coach spacings, train nose, pantographs and bogies[1-6], exceeds rolling noise and becomes the primary contributor to high-speed train noise above approximately 350 km/h.[4] Among these sources, the bogies contribute the greatest sound power[4]. Therefore, comprehending the generation mechanisms of bogie noise is crucial for controlling overall aerodynamic noise from high-speed trains. However, the

complex geometry and intricate incoming flow pose significant challenges, making both experimental and numerical investigations of bogie noise extremely difficult.

Although field tests with microphone arrays can be used to localise noise sources[7], they cannot readily separate the bogie aerodynamic noise from rolling noise. Additionally, field tests pose challenges such as high measurement costs and difficulties in arranging appropriate tests. Wind tunnel tests, another option, face limitations in replicating the velocity profile beneath a train, especially in low-noise wind tunnels lacking a moving ground. Uda et al. [8] addressed this by employing an array of hot-wire probes on the track slab to capture the velocity distribution beneath a moving train. Their findings revealed higher flow speeds beneath the front bogie compared to the rear ones due to boundary layer growth beneath the train floor. To simulate this, they adjusted the velocity profile in a wind tunnel beneath a 1/7th scaled model train to match that of an operational train.

Also in a wind tunnel test, Latorre Iglesias et al. [9] investigated the aerodynamic noise generated by motor and trailer bogies at 1/7 scale. They found that both configurations exhibited similar noise spectra, which can be attributed to nearly identical components exposed to the incoming flow, while internal components shielded by the bogie cavity contributed less to the overall noise. Similarly, Sawamura et al. [10] conducted experiments using a 1/7 scaled model in a wind tunnel, positioning a two-dimensional (2D) microphone array beneath the bogie to identify source regions. They found primary noise sources at low frequencies towards the rear of the bogie. Yamazaki et al. [11] installed a 2D microphone array at the trackside using another 1/7 scaled model in a wind tunnel, and estimated noise contributions from components inside the bogie cavity by arranging various components within it. Despite revealing phenomena and characteristics of bogie noise generation, experimental results have not fully revealed underlying mechanisms, necessitating numerical simulations to address these limitations.

Simulating bogie aerodynamics, especially aeroacoustics, presents significant challenges due to the complex geometry and complicated flow phenomena. When choosing a simulation approach, it is crucial to consider the required flow field information, turbulence model requirements, and computational resources. Grid

resolution, especially in the boundary layer around the structure, must meet criteria specified by the chosen turbulence models.

Zhang et al. [12] and Wang et al. [13] utilized the Detached Eddy Simulation (DES) method to investigate the influence of the shape of the bogie and its cavity on the surrounding flow structure and the aerodynamic performance of a high-speed train. Liang et al. [14] studied the characteristics of the aerodynamic noise of the leading car of a high-speed train using Large Eddy Simulation and the Ffowcs-Williams and Hawkings (FW-H) analogy. Although several numerical investigations have explored whole train models incorporating bogies[12-19], most focus on the overall flow field without providing detailed grid information or flow characterization of the bogie region. Discretizing a bogie with complex geometry for Computational Fluid Dynamics (CFD) simulations appears to be a bottleneck, prompting the simplification of bogie geometry as an alternative. In a step towards modelling a simplified bogie, Zhu et al. [20] simulated an isolated wheelset of a high-speed train at 1/10 scale, revealing tonal noise due to vortex shedding from both the axle and wheel. Subsequently, the model was expanded to include tandem wheelsets before progressing to a simplified bogie configuration with tandem wheelsets linked via a highly simplified bogie frame composed of two parallel square bars. Finally, the simplified bogie was placed in a cavity [21-23]. Once the model was installed in the cavity of the bogie, the tonal vortex shedding was largely suppressed and the noise became broadband. Subsequently, Li et al. [24] placed the simplified bogie under a simplified car body to study the noise generation mechanisms of a leading car.

As mentioned above, there are two crucial issues about these numerical simulations. In some studies, the boundary layer grid, which is critical for accurate flow separation assessments[25-27], lacks sufficient refinement. In others, the bogie geometry lacks details. Thus, there is an urgent need to explore a practical approach that combines a sufficiently fine yet affordable CFD grid for discretizing the bogie with realistic geometry, including all main components and features.

In three-dimensional (3D) CFD models, structured, unstructured, and hybrid grids are commonly used for discretization. Structured grids, aligned with the flow, enhance accuracy and convergence but are difficult to generate for complex geometries[22, 28-30]. Unstructured grids, using tetrahedral or polyhedral cells, offer flexibility and can be generated automatically. Polyhedral grids have advantages such as

better gradient approximation and reduced computational resource requirements compared to tetrahedral grids[29, 31-33]. A hybrid grid, combining structured and unstructured grids, has been successful in various applications[34-36] but has not been widely applied to train bogies.

In this study, a practical numerical approach is developed to predict the aerodynamic noise generated by a high-speed train bogie. It involves scaling and constructing the bogie model, generating a hybrid grid, simulating flow fields and acoustic radiation, and scaling the acoustic results. In most studies using conventional hybrid grids[34-36], both the structured and unstructured grids may exist in both the boundary layer region and the far field volume as these are generated automatically by the commercial software. However, the mesh quality, especially in the boundary layer region, cannot be ensured in models with complex geometries. Unlike these conventional hybrid grids, in the present work a fully structured hexahedral grid is established near the model surfaces, while an unstructured polyhedral grid fills the rest of the volume. This ensures that the quality of the boundary layer grid is guaranteed, while the unstructured grid in the volume retains its flexibility. The methodology for generating this hybrid grid is explored. Additionally, the flow field around the bogie and the noise generation mechanism are investigated, providing insight into bogie noise generation for future numerical studies.

2. Model geometry and numerical settings

The bogie model depicted in Figure 1 retains all major components to ensure a realistic bogie geometry, including wheelsets, motors, gearboxes, axle boxes, dampers, air springs, frame, and bolster. However, minor features are simplified; for example, the wheels are represented by discs, neglecting the flange and the smaller thickness in the wheel web region. Similar simplifications are applied to axles, motors, gearboxes, and damper end plates. Components beneath the bolster beam, such as the traction block and lateral dampers, are substituted with a single block with equivalent blockage ratio.
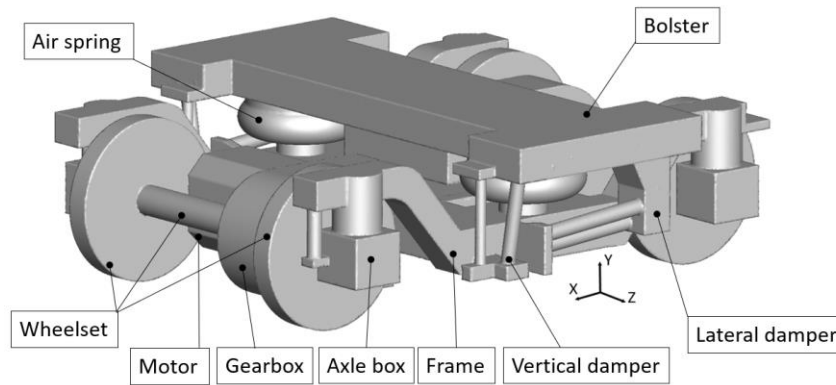
Figure 1 The 3D model of the bogie

The primary aim of this research is to explore the utilization of a hybrid grid system to facilitate affordable numerical simulations for flow around a bogie with complex geometry. To simplify computations, the influence of the train nose on incoming flow is neglected and the bogie is placed in a simplified cavity, as shown in Figure 2.

To minimize the computational cost, the speed of the flow was set to 10 m/s and the bogie model was downscaled to a 1:12 scale, resulting in a Reynolds number (UD/v, where U is the freestream velocity, D is a typical dimension, and v is the molecular viscosity) of 1.91×10^5 based on the width of the car body W_0 (0.287 m). This falls within the Reynolds number range investigated by Lauterbach et al. [5], who observed that the noise produced by the front bogie exhibited only a minor dependency on the Reynolds number in the range 1.53×10^5 to 3.7×10^6. The coordinates of the train are adopted, in which the train remains stationary, whereas the ground and the incoming flow move in the opposite direction at the operational speed of the train. The coordinate origin is situated at the centre of the bogie, aligned with the mid-plane and positioned at the same level as the centres of the wheels.
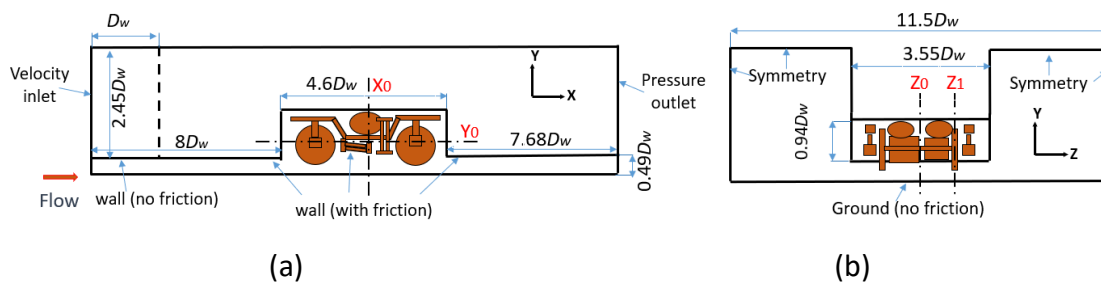

(a)

(b)

Figure 2 Sketches of the bogie in a simplified cavity (not to scale). D_w is the wheel diameter. (a) Side view, (b) End view.

Figure 2 also shows the boundary conditions used in the simulations. Ground friction effects are neglected, so a free-slip boundary condition is applied to the ground. Top and side domain boundaries are set as symmetry. A constant velocity (10 m/s) is applied at the inlet, and a pressure outlet boundary condition is used at the outlet with zero gauge pressure. The inlet extends $8D_w$ upstream, where D_w is the diameter of the wheels. To stabilize the simulation, a free-slip wall is used over a length of D_w after the inlet, with a no-slip wall over the remaining length of $7D_w$. The downstream length is set to $7.68D_w$, and lateral domain size to $11.5D_w$. These are carefully selected to ensure that the downstream outlet and side boundary conditions do not affect the flow in the bogie region. The distance between the simplified car body bottom and ground is approximately $0.49D_w$. A gap of 250 mm ($0.33D_w$) is maintained between the ground and the bottom of the wheels.

Considering that the Mach number is less than 0.3, the solution to the incompressible 3D unsteady Navier–Stokes equations is obtained, using Delayed DES (DDES) with the Spalart-Allmaras (S-A) turbulence model[37, 38]. Prior to the unsteady simulation using DDES, a Reynolds-averaged Navier–Stokes (RANS) simulation employing the S-A turbulence model was performed to establish the initial flow field.

3.   Hybrid grid generation and validation

Predicting aerodynamic noise requires a high-quality computational grid because the signals relevant to the noise are only a small portion of the turbulence and are susceptible to numerical errors[39]. The hybrid grid is generated by first creating a high-quality structured grid with hexahedral cells near solid surfaces using ANSYS IcemCFD 14.1. Next, an unstructured tetrahedral grid is created for the remaining domain and merged with the hexahedral grid at an interface region. Finally, using ANSYS Fluent 14.8, the tetrahedral grid is converted to a polyhedral grid, which is less sensitive to stretching [31] and contains a smaller number of cells than the tetrahedral one.

3.1 Validation of the hybrid grid strategy

Before meshing the bogie shown in Figure 1, simulations were conducted of flow over circular and approximately square cylinders to validate the hybrid grid generation procedure and establish appropriate numerical settings. The Reynolds number is 10^5 for

the circular cylinder (based on the cylinder diameter D=0.05 m) and 8.2×10⁴ for the square one (based on the side width of the square cylinder D=0.041 m).

Comparisons are made between two types of grid for discretising the flow over circular and square cylinders. Grid type I corresponds to a structured grid from Liu[40], with all grid parameters similar to those utilized in that study. Grid type II employs a hybrid approach, utilizing the same near-wall structured grid parameters and a polyhedral grid for the rest of the domain. Cases c-I and c-II represent the circular cylinder with grid types I and II, while s-I and s-II represent the square cylinder with grid types I and II. Figure 3 displays the hybrid grid (type II) distribution near the cylinders.

Identical to the studies from Liu[40], the computational domain of the circular cylinder is 30D × 20D ×3D, while that for the square cylinder case is 30D x 20D x 4D. The cylinder's centre is positioned 10D from the inlet boundary. The boundary conditions for the circular cylinder case can be found in reference[41] and those for the square cylinder can be found in reference[42]. There are 2.5 million cells for case c-I, 1.86 million for case c-II, 2.2 million for case s-I and 1.47 million for case s-II.
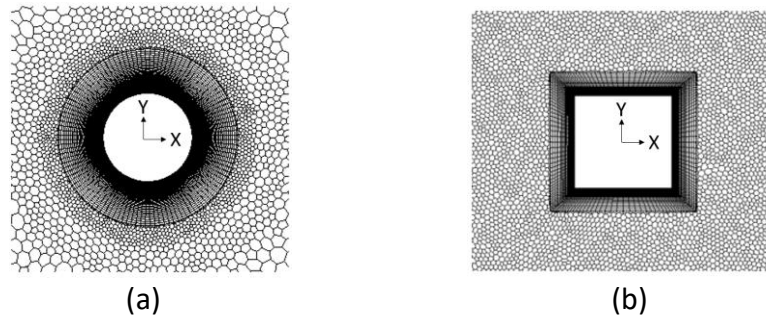

(a)   (b)

Figure 3 Details of the hybrid grid system used for cylinder flow. (a) Hybrid grid around circular cylinder (case c-II), (b) hybrid grid around square cylinder (case s-II).

Table 1 lists various parameters summarising the flow for the circular cylinder. C_d is the mean drag coefficient ($C_d = \frac{F_{drag}}{0.5\rho U_\infty^2 DL}$, where F_{drag} is the drag force, ρ is density of air, U_∞ is the freestream velocity (30 m/s), D is the cylinder diameter and L is its length). $C_{l,rms}$ is the root-mean-square (rms) value of the lift coefficient ($C_l = \frac{F_{lift}}{0.5\rho U_\infty^2 DL}$, where F_{lift} is the lift force). St is the Strouhal number corresponding to the frequency f of vortex shedding ($St = \frac{fD}{U_\infty}$). The flow separates from the cylinder at an angle θ_{SEP} measured from the front stagnation point.

Table 1 shows that deviations between the current results and published data are within 6%, except for $C_{l,rms}$, which is sensitive to simulation and experimental conditions. Comparing the results of case c-I and case c-II, the differences in the mean drag coefficient C_d and separation angles θ_{SEP} are less than 1% , while the differences in St and $C_{l,rms}$ are under 2.5%. This indicates that comparable performance is achieved by hybrid and structured grids.

Table 1 Comparison of results for circular cylinder at $Re = 10^5$

Grid Type	Case	C_d	$C_{l,rms}$	St	θ_{SEP} (°)
Structured	c-I	1.16	0.580	0.185	82.0
Hybrid	c-II	1.17	0.563	0.192	82.5
Num.	Liu[40]	1.23	0.73	0.19	84.0
Exp.	Schewe[43]	1.21	0.29	0.20	-
Exp.	Norberg[44]	-	0.51	0.19	-
Error (%)	Err. of c-I	5.7	20.5	2.6	2.3
	Err. of c-II	4.9	22.8	1.0	1.9

In Table 2, the differences in C_d and $C_{d,rms}$ between case s-I and the results of Liu[40] are approximately 14% and that for $C_{l,rms}$ is about 7%. The simulated results from Liu[40] incorporated round corners on the cylinder with a radius of 0.5 mm, utilizing a finely tuned grid near these corners, which improves alignment with the experimental data. The results of s-I and s-II are very close to each other. A hybrid grid case with rounded corners (s-IIa) was also computed, utilizing grid parameters similar to those of case s-II. The results of case s-IIa show closer agreement with both the experimental data and numerical results from Liu[40] than the other two cases featuring sharp corners. However, to simplify grid generation for subsequent bogie component simulations, rounded corners will not be used.

Table 2 Comparison of results for square cylinder at $Re = 8.2 \times 10^4$

Grid Type	Case	C_d	$C_{d,rms}$	$C_{l,rms}$	St
Structured	s-I	2.39	0.238	1.48	0.130
Hybrid	s-II	2.38	0.195	1.47	0.130
Hybrid	s-IIa	2.06	0.199	1.39	0.128
Num.	Liu[40]	2.08	0.210	1.38	0.129
Exp.	Vickery[45]	2.05	0.170	1.30	0.120
Exp.	Norberg[46]	2.10	-	-	0.130
	Err. of s-I	14.9	13.3	7.2	0.8
Error (%)	Err. of s-II	14.9	15.2	7.2	0.8
	Err. of s-IIa	1	5.2	0.7	0.8

Pressure data sampled on the square cylinder surface was input into the FW-H equation to compute far-field noise[47], with receivers positioned at the cylinder mid-span, 5 m radially from the axis. Figure 4 shows the one-third octave band spectrum of the sound pressure level (SPL) and the angular distribution of the overall sound pressure level (OASPL) computed using the hybrid grid. These results are compared with the numerical and experimental results of Liu[40]. The experimental data have been rescaled to match the numerical conditions. Figure 4(a) shows the noise spectra corresponding to a receiver positioned perpendicular to the flow direction, i.e. at $\theta = 90°$. A good agreement is found between the peaks. Figure 4(b) plots the overall level against angle. The current results are slightly higher than the numerical result from Liu[40], with a maximum deviation of approximately 1 dB.

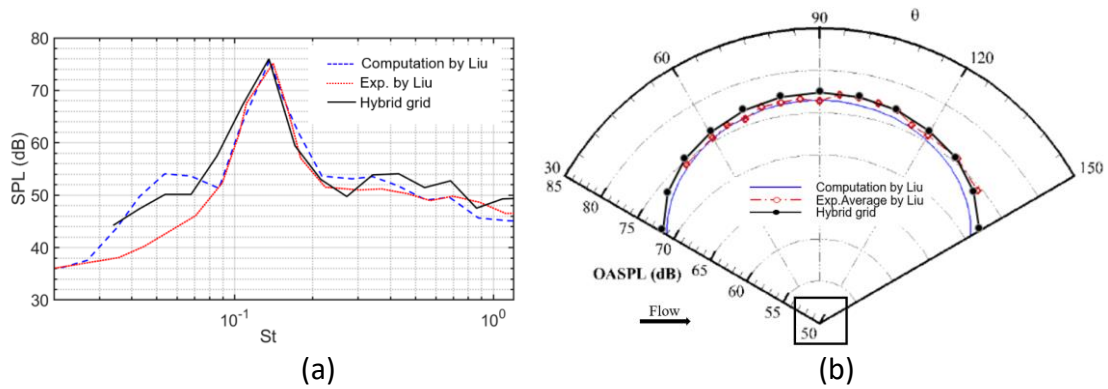(a)   (b)

Figure 4 The aerodynamic noise of the square cylinder at $Re = 8.2 \times 10^4$; the experimental data from Liu[40] are scaled to correspond to the numerical conditions. (a) noise spectra at 90° (1/3 octave); (b) directivity.

3.2 Hybrid grid generation of bogie model

To create the hexahedral boundary layer grid for the bogie, the bogie was segmented into five distinct parts based on their geometric attributes, as illustrated in Figure 5(a) to (e). Different surface grid sizes were specified for these five parts according to the local flow conditions. The boundary layer grid was generated using hexahedral grid generation blocks covering the solid surface in ANSYS IcemCFD 14.1. The parameters of the boundary layer will be presented in the grid dependence study in Section 3.3 below. After generating the hexahedral grid, a tetrahedral grid was used to fill the remaining volume of the computational domain. The volume grid in the cavity was refined with a grid refinement region. Once the hexahedral and tetrahedral grids

were connected, ANSYS Fluent 14.1 was used to convert the tetrahedral grid into a polyhedral grid, reducing the number of cells by half and improving grid quality[31].

<div align="center">(a)   (b)   (c)</div>

<div align="center">(d)   (e)</div>
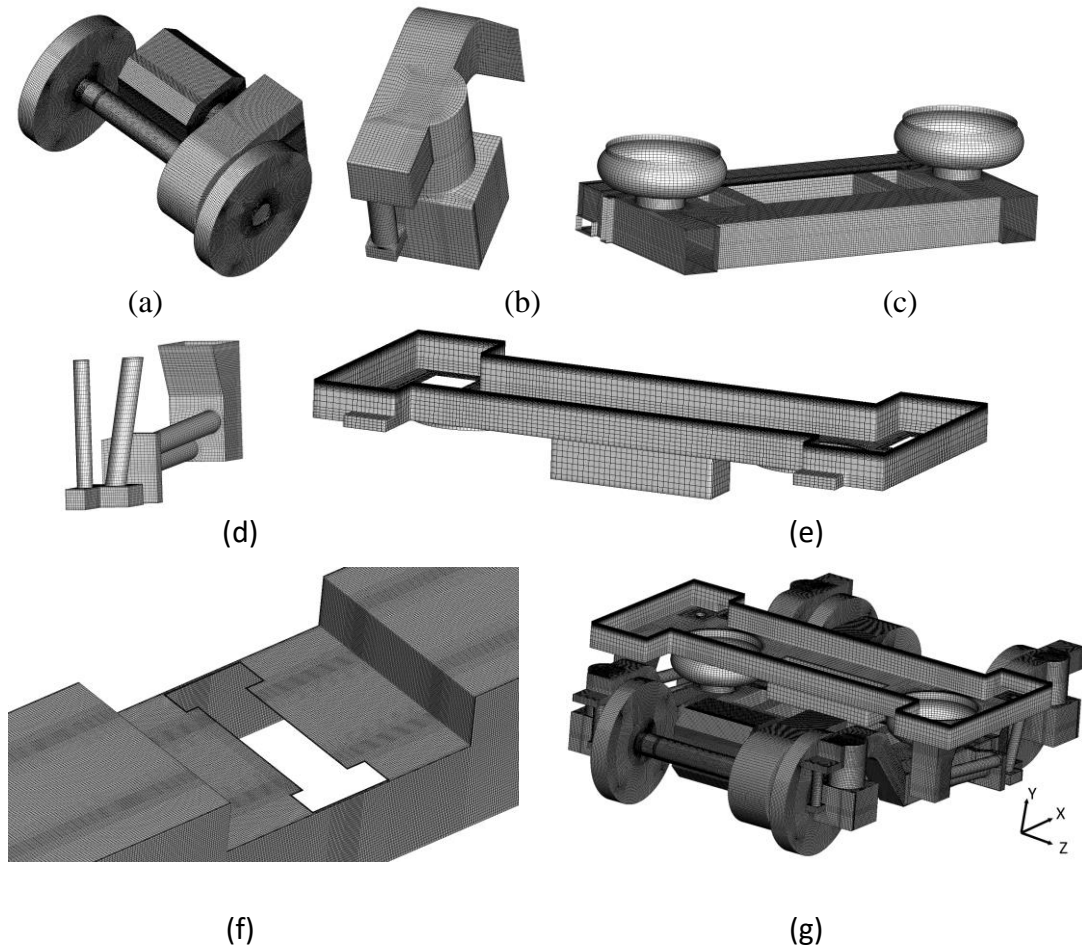
<div align="center">(f)   (g)</div>

Figure 5 Surface mesh distribution of model components. (a) Wheelset (including motor and gearbox); (b) axle box; (c) frame components; (d) side yaw dampers; (e) bogie bolster beam; (f) cavity; (g) whole bogie.

Different slices, denoted by the dash-dot lines in Figure 2, are used to illustrate the grid. Figure 6 displays the grid distribution on the slices Z_0 and Y_0. In the boundary layer, to ensure a high resolution, the grid is designed with the highest density in the structured grid near the solid surfaces. As seen in Figure 6(a), the density of the volume grid is chosen to be greater around the bogie than in other areas because the velocity has greater variation in this region.
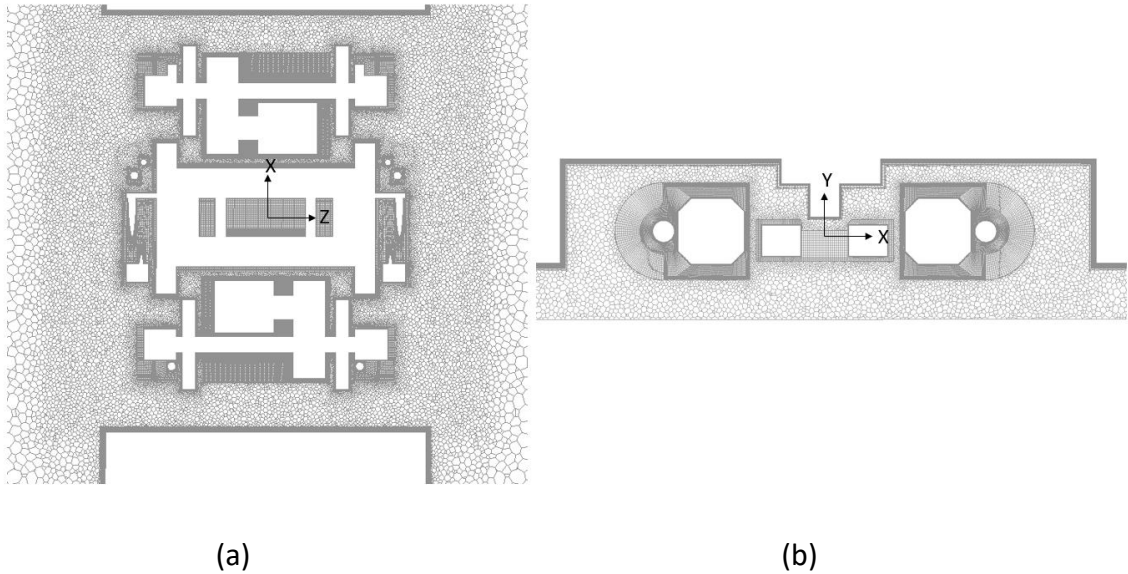
<div align="center">(a)   (b)</div>

Figure 6 Mesh distribution on solid surface at the slices defined in Figure 2. (a) Slice Y_0; (b) slice Z_0.

3.3 Grid sensitivity study

To establish an appropriate grid resolution for the bogie model shown in Figure 1, a grid sensitivity study was performed for a simpler model. This model omitted some components (the bolster, motors, and gearboxes) and modified the side dampers' end plates to flat plates. Due to the symmetry of the simplified bogie, a half-width model was used, with boundary conditions identical to Figure 2, except the middle plane was designated as a symmetry boundary condition.

Table 3 presents details of the grid for the four cases established for the grid study. In the boundary layer region, the parameters of the hexahedral grid remained constant perpendicular to the wall, while the grid sizes in the other two directions were refined by adjusting the aspect ratio. The non-dimensional height of the first cell (y^+) on all solid walls was kept below 1. The boundary layer grid consisted of 25 layers with an expansion ratio of 1.1. Case medium-2 was created to evaluate the grid aspect ratio within the cavity, differing from case medium-1 only in the grid size in the cavity region. The volume grid in the area around the bogie, where intense turbulent flow is expected, was refined progressively at a ratio of 1.4 between the coarse, medium, and fine cases. To mitigate the impact of the time step size, the maximum CFL value for all calculations was kept below 5. A detailed time-step sensitivity study can be found in He[48].

Table 3 Summary of the main grid information

Components	Parts	Fine	Medium-1	Medium-2	Coarse
		Maximum aspect ratio			
Drive system	Wheelset	56	80		112
Bearing component	Axle box	48	65		90
	Front damper	80	110		150
Frame component	Frame	90	125		180
	Air springs	55	80		112
Side dampers	Vertical damper	80	112		160
	Lateral damper	90	128		176
Cavity		105	148	200	210
Total number of cells (million)		18.1	9.6	8.1	4.8

Figure 7 illustrates the time-averaged drag and lift force coefficients for both the bogie and the cavity, using the full cross-sectional area of the train (0.0826 m² in the 1/12th scaled model) as the reference area. The medium-1 and medium-2 cases show mean values within 5% of the fine case, while the coarse case has more pronounced deviations, except for the lift coefficient of the cavity. Therefore, the grid parameters of medium-1 and medium-2 are more suitable than those of the coarse case. For the full bogie model discretization, the medium-1 grid parameters are preferred. However, due to the complexity in the vicinity of the bogie bolster beam, as shown in Figure 5 (e), adjustments are made to enhance local mesh quality, resulting in actual mesh sizes within the cavity varying between the medium-1 and medium-2 cases.
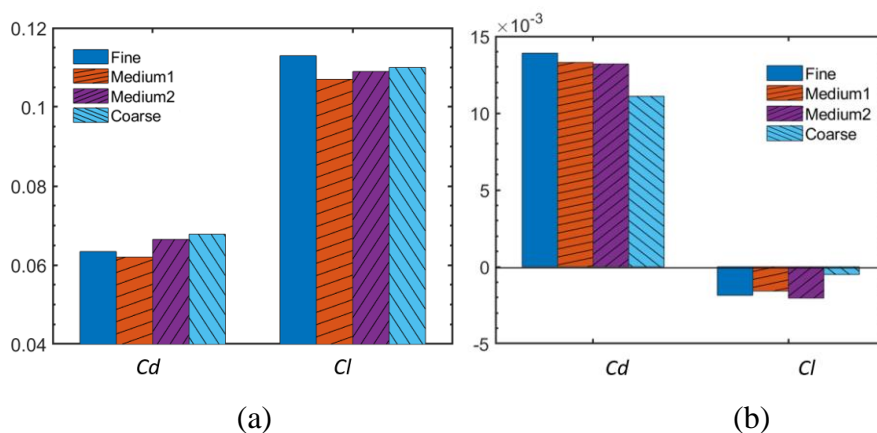

(a)   (b)

Figure 7 Summary of force coefficients from different cases. (a) Cavity, (b) bogie.

4. Numerical results and discussion

The grid parameters chosen in Section 3.3 are implemented in the subsequent simulations for the full bogie and cavity model depicted in Figure 1 and Figure 2. Based on these grid parameters, the full model has about 23.8 million cells. A time step size of 1.5×10^{-5} s is selected to ensure the maximum CFL remains smaller than 5. The total simulation time is approximately 5.6 s, which corresponds to 36 flow-through times of the computational domain. The wall-time of the simulation is around 1120 hours when employing 512 processors on the Iridis4 high performance computer at the University of Southampton.

4.1 Aerodynamic results
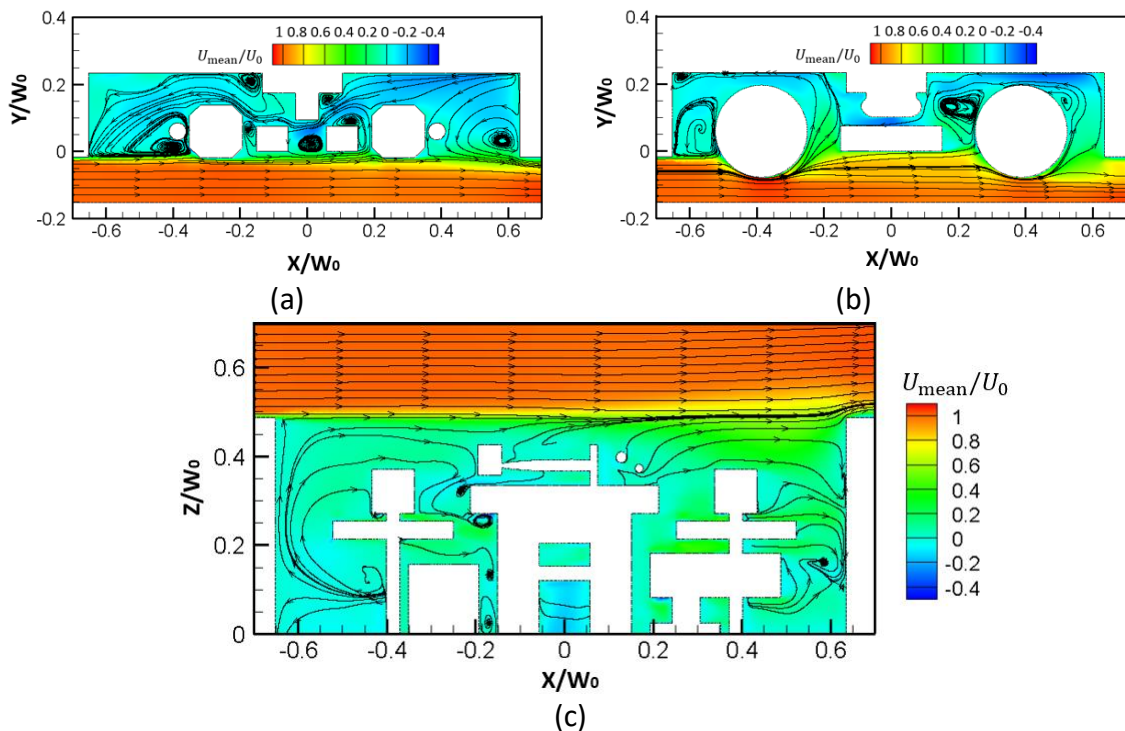
Figure 8 Contours of time-averaged streamwise velocity alongside the 2D mean streamlines., W_0 is the width of the cavity. (a) slice Z_0; (b) slice Z_1; (c) slice Y_0 (half-width is shown).

To investigate the noise generation mechanism, analyses are conducted on the time-averaged velocity field, instantaneous vorticity fields, and wall pressure fluctuations. Figure 8 presents contours of the mean streamwise velocity across three slices (as indicated in Figure 2), overlaid with 2D mean streamlines. In general, the flow predominantly enters the cavity from the bottom. Within the bogie cavity, the flow

exhibits notably lower velocity, recirculating gradually from the rear to the front through the upper section of the cavity. Moreover, the bottom and sides of the bogie are exposed to flow with higher speeds than the components inside the cavity.
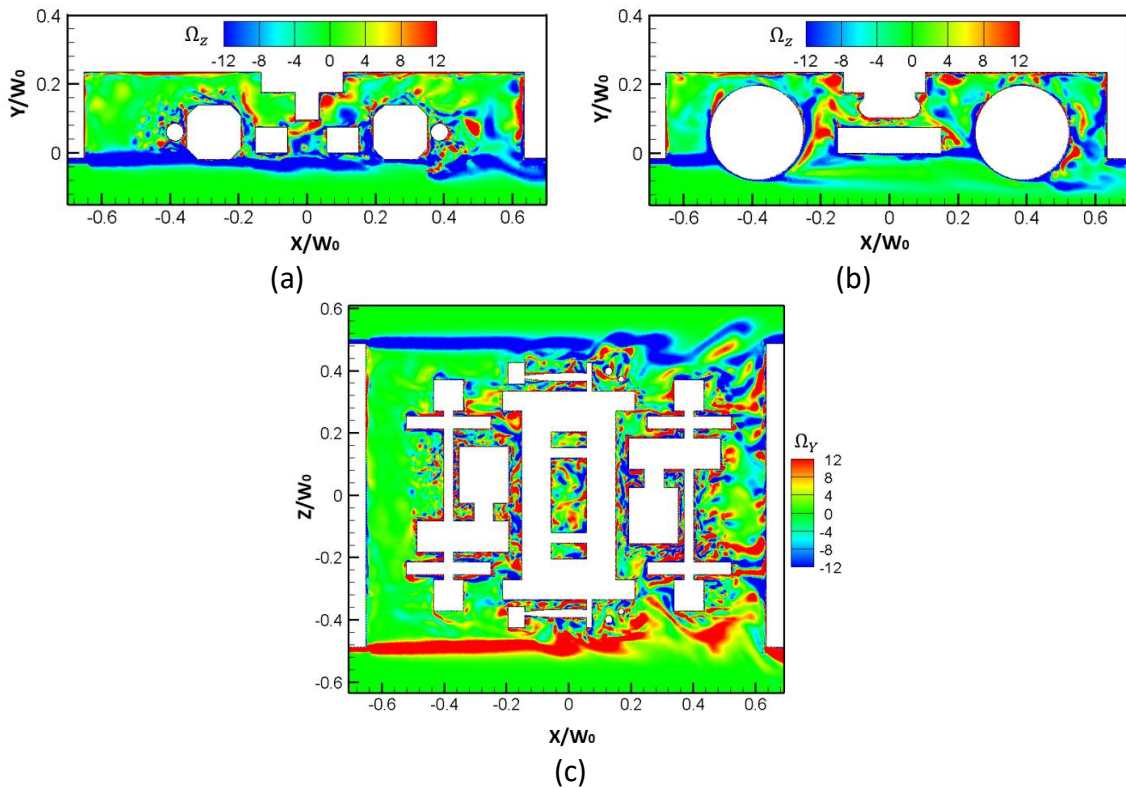

Figure 9 Contours of instantaneous vorticity field, W_0 is the cavity width. (a) Ω_z on slice Z_0; (b) Ω_z on slice Z_1; (c) Ω_Y on slice Y_0.

Figure 9 displays the contours of the instantaneous vorticity (Ω) across the same three slices. It can be observed that the shear flow detaches from the cavity leading edge, a phenomenon consistent with findings in the simulations conducted by Zhu et al. [22]. This flow then impinges on the lower sections of the cavity trailing edge and the bogie. However, unlike the results of Zhu et al. [22], after detaching from the upstream cavity edge, the shear layer does not bend and penetrate into the cavity. Instead, it travels downstream and interacts with certain components, such as the side dampers and the bottom of the bogie. This disparity compared with the results of Zhu et al. [22] can be largely attributed to the differences in geometrical configurations, e.g. additional components in the cavity, the different height of the floor above the ground, and the greater blockage ratio of the shielded part of the bogie. Subsequently, the interaction with the bogie causes the detached shear layer to disperse in the downstream direction, leading to a portion of it impacting the rear surface of the cavity. Morris[49] highlighted

that in shallow open cavities, the dipole noise is produced by the unsteady pressure fluctuations on the cavity surface caused by the detached shear layer. This principle similarly applies to the model depicted in Figure 2. The pressure fluctuations resulting from the interaction between the detached shear layer and the solid surfaces of the model could serve as potential sources of the dipole noise.
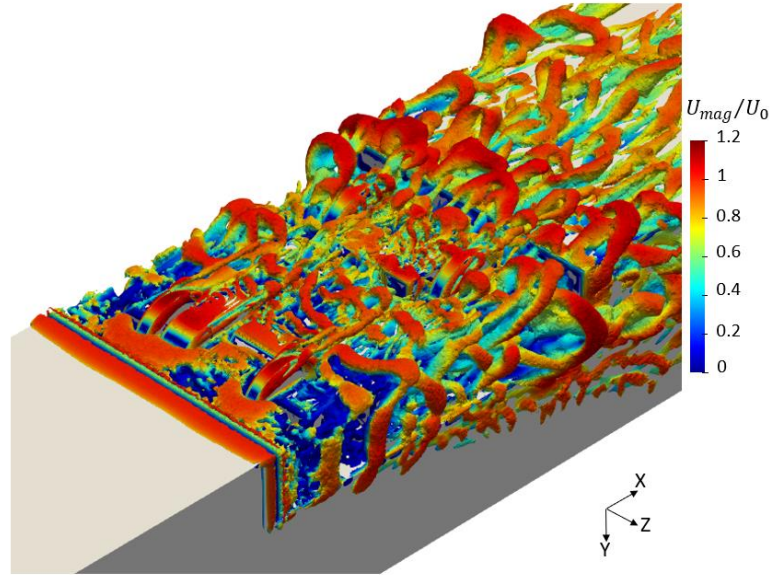

Figure 10 Vortex structures represented by $Q/(U_0/W_0)^2$ at a value of 3, coloured by U/U_0.

In Figure 10, the vortex structures are visualized by iso-surface of the non-dimensional quantity $\bar{Q} = Q/(U_0/W_0)^2$ and coloured by velocity ratio, U_{mag}/U_0. Here Q is the second invariant of velocity gradient, U_{mag} is the local instantaneous velocity magnitude, U_0 is the free stream velocity and W_0 is the width of the train body (0.287 m in scaled size). The iso-surface is plotted for $\bar{Q} = 3$. It can be noted that the sides and bottom of the bogie are covered by vortices shed from the upstream rim of the cavity. This vortical flow interacts with the bottom and side components until it is hindered by the rear surface of the cavity. Areas impacted or flushed by the vortical flow have high surface pressure fluctuations which, in turn, could generate aerodynamic noise.

To establish a connection between the flow behaviour and aerodynamic noise sources, an investigation into the distribution of the pressure fluctuations on the solid surfaces was conducted. The rms value of the rate of change of pressure, dp/dt , on the solid walls serves as an indicator of dipole noise sources. Its magnitude can be employed

to quantify the noise source intensity [50]. To obtain the value over a specific frequency range, this is calculated in decibels as

$$L_{\dot{p}} = 10 \log_{10}(\sum_{i=1}^{n} PSD_i \times df)$$

(1)

where PSD_i is the signal power spectral density of dp/dt at the ith frequency, df is the frequency interval and n is the number of frequencies considered, which is set to correspond to the range from 20 to 1000 Hz.

To quantify the strength of the total noise source of a component, the power of every surface element of the component is summed:

$$L_{\dot{p},total} = 10 \log_{10}\left(\sum_{j=1}^{m}(\sum_{i=1}^{n}(PSD_{ij} \times df) \times dA_j) \right)$$

(2)

where m is the total number of grid elements associated with the component, and dA_j is the area of the jth grid element.

During the simulation, the pressure signals from the surface grid elements were collected (totalling approximately 1.12×10^6) over a duration of approximately 5 s. The PSD of each surface element was calculated using Welch's method with a Hanning window. The signal was divided into 25 segments with a 50% overlap and a segment length of 0.4 s, resulting in a frequency resolution of 2.5 Hz. Figure 11 displays the distribution of $L_{\dot{p}}$ on the model surfaces.

Figure 11(a) plots the noise source distribution on the surfaces of the whole model. In general, the strength of $L_{\dot{p}}$ is more significant on the bottom surfaces, particularly at the rear section of both the cavity and the bogie. This observation agrees well with the findings of Sawamura et al. [10], who similarly noted that the most prominent sound sources are situated at the rear portion of the bogie. Based on the observations in Figure 8 and Figure 9, the detached shear layer impinges on the front part of the bogie, while a wake with strong turbulence impinges on the rear components, resulting in strong noise sources at the rear, as found in Figure 11(b). Figure 11(c) displays the distribution of $L_{\dot{p}}$ on the cavity surface. A prominent noise source is evident at the rear wall of the cavity, particularly at its corners and along the edges of the bottom surface. Besides the detached shear layer originating from the upstream edge of the cavity, these areas of significant pressure fluctuations are also influenced by the incoming wake flow

from upstream. Figure 8(a) illustrates how the rear wall of the cavity allows some of the upstream wake to infiltrate into the cavity. Consequently, as shown in Figure 11(b) and (c), the area of strong noise sources extends to the upper part of both the cavity and the bogie. The overall level of the rate of change of pressure $L_{\dot{p}\_total}$, as given by Equation (2), is 2.3 dB higher on the bogie surface than on the cavity surface. However, it is important to note that when calculating $L_{\dot{p}\_total}$, phase information is not considered. Consequently, the far field noise level originating from the cavity may not necessarily be lower than that from the bogie. This is investigated in the next section.
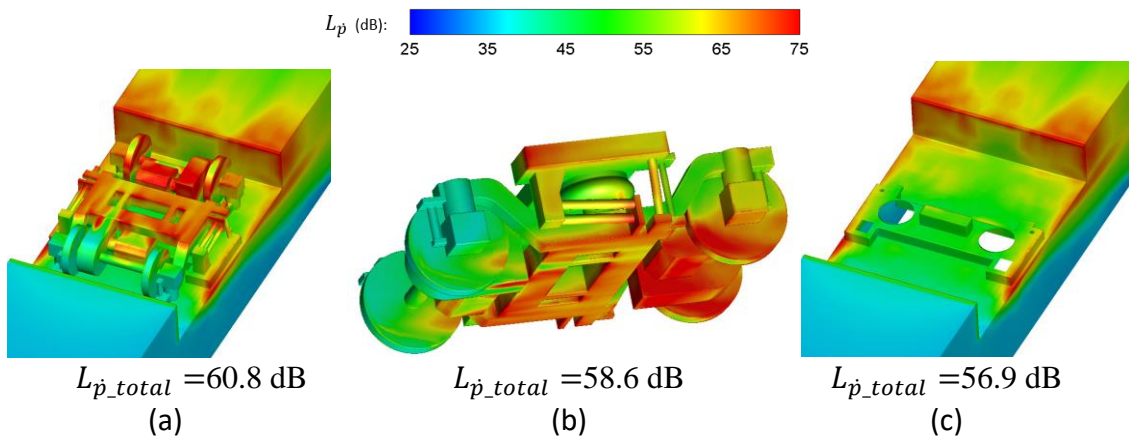

$L_{\dot{p}\_total}$ =60.8 dB $L_{\dot{p}\_total}$ =58.6 dB $L_{\dot{p}\_total}$ =56.9 dB

(a)   (b)   (c)

Figure 11 Contours of the pressure rate of change, dp/dt, on the components integrated from 20 to 1600 Hz. (a) Bottom view of the whole model; (b) bogie; (c) bottom view of the cavity.

To investigate the characteristics of noise sources in different frequency regions, Figure 12 to Figure 15 display the contours of $L_{\dot{p}}$ on the cavity and bogie calculated by equation (1) for different frequency bands. As mentioned in the introduction section, the noise generated by a bogie is dominated by low frequencies. Therefore, the frequency bands are initially obtained by uniformly dividing the frequencies below 600 Hz. Then, another division for finer resolution is conducted based on the results of the first division. Since the lowest frequency of interest is 20 Hz, the lower limit of the first bands is specified as 20 Hz.

The pressure fluctuation on the cavity walls in the frequency range 20-200 Hz, shown in Figure 12(a), has the greatest power and has a noise source distribution similar to that shown in Figure 11(a). The value of $L_{\dot{p}\_total}$ is also largest compared with the two higher frequency ranges. This indicates that, for the noise sources distributed on the cavity walls, the pressure fluctuation in 20-200 Hz has the greatest contribution. To

investigate the noise source distribution in this frequency region further, the pressure fluctuation is divided into three smaller segments, as shown in Figure 13. The results show that the pressure fluctuation in the region 60-120 Hz has a strong noise source. The noise source at the edge of the cavity rear wall is stronger than in other areas because of the impingement of the shear flow from upstream, as shown in Figure 9(a) and (b).

Figure 14 and Figure 15 depict the corresponding results for the bogie surface. Although the value of the overall noise source strength, $L_{\dot{p}\_total}$, is greatest in the frequency band 20-200 Hz, the strength of the pressure fluctuations on the rear part of the bogie underside is similar to that in the high frequency bands 200-400 and 400-600 Hz. It is believed that this is because the wake flow from upstream components, shown in Figure 9(a) and (b), has smaller eddies and thus more uniform energy distribution across the frequency range than that of the detached shear layer from upstream. This also explains the similar distribution of pressure fluctuation within the smaller frequency range in Figure 14(b) and (c).

From the above analysis of the noise sources in different frequency bands, it can be concluded that the pressure fluctuation has the greatest contribution from the low frequencies (20-200 Hz) both for the cavity and bogie. This finding is consistent with the experimental studies from Latorre Iglesias et al. [9] and Sawamura et al. [10] which also found the noise at low frequencies is dominant for the bogie region.

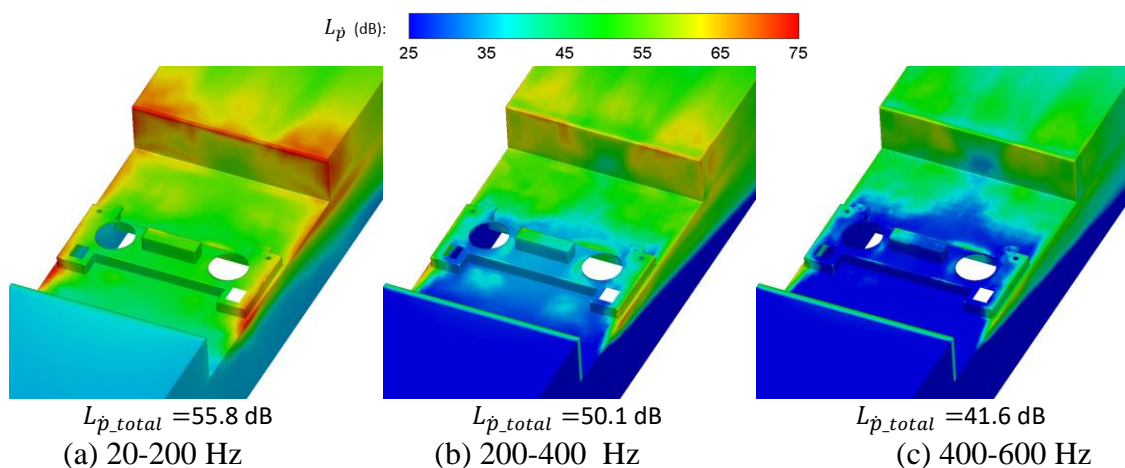| $L_{\dot{p}\_total}$ =55.8 dB	$L_{\dot{p}\_total}$ =50.1 dB	$L_{\dot{p}\_total}$ =41.6 dB
(a) 20-200 Hz	(b) 200-400 Hz	(c) 400-600 Hz

Figure 12 Surface contours of the pressure rate of change dp/dt on the cavity integrated over three ranges between 20 and 600 Hz (bottom view)
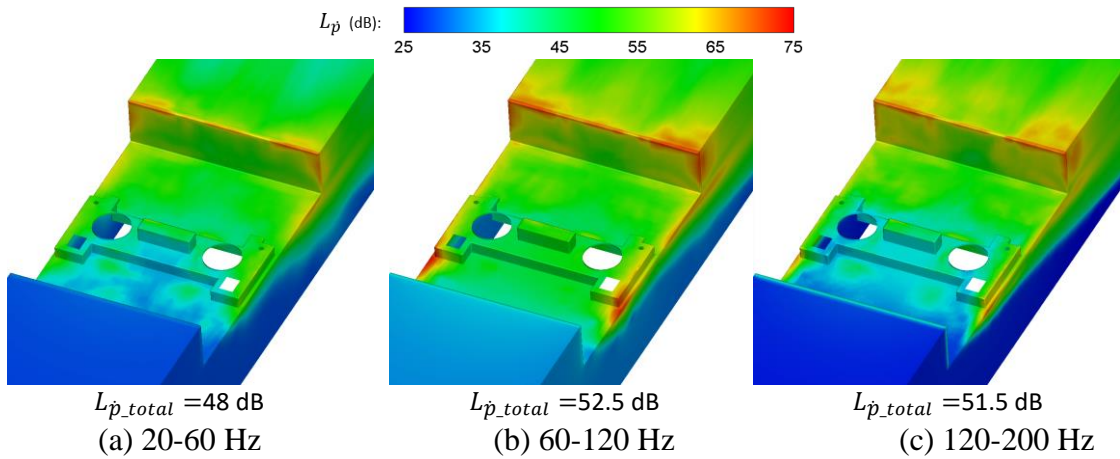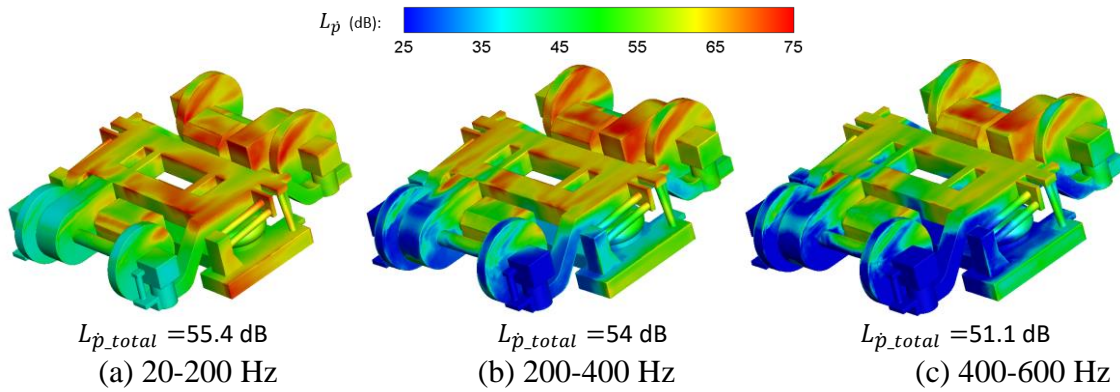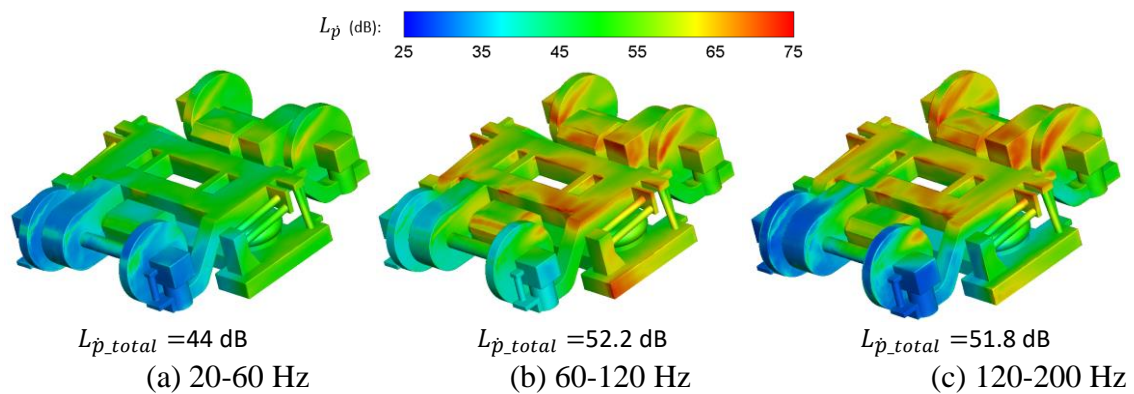
$L_{\dot{p}\_total}$ =48 dB
(a) 20-60 Hz

$L_{\dot{p}\_total}$ =52.5 dB
(b) 60-120 Hz

$L_{\dot{p}\_total}$ =51.5 dB
(c) 120-200 Hz

Figure 13 Surface contours of the pressure rate of change dp/dt on the cavity integrated over three ranges between 20 and 200 Hz (bottom view)

$L_{\dot{p}\_total}$ =55.4 dB
(a) 20-200 Hz

$L_{\dot{p}\_total}$ =54 dB
(b) 200-400 Hz

$L_{\dot{p}\_total}$ =51.1 dB
(c) 400-600 Hz

Figure 14 Surface contours of the pressure rate of change dp/dt on the bogie integrated over three ranges between 20 and 600 Hz (bottom view)

$L_{\dot{p}\_total}$ =44 dB
(a) 20-60 Hz

$L_{\dot{p}\_total}$ =52.2 dB
(b) 60-120 Hz

$L_{\dot{p}\_total}$ =51.8 dB
(c) 120-200 Hz

Figure 15 Surface contours of the pressure rate of change dp/dt on the bogie integrated over three ranges between 20 and 200 Hz (bottom view)

4.3 Aeroacoustic results

The sampled time-dependent surface pressure data are used as input for the FW-H equation to calculate the far-field noise. The sound pressure level (SPL) obtained from the scaled simulation is converted to the SPL at full-scale by adding the following correction:

$$\Delta SPL = 10 \log_{10}\left[\frac{\left(\frac{D_1}{D_2}\right)^2 \left(\frac{U_1}{U_2}\right)^6}{\left(\frac{r_1}{r_2}\right)^2}\right] \tag{3}$$

where D_1/D_2 is the geometry ratio, U_1/U_2 is the velocity ratio and r_1/r_2 is ratio of the receiver distance. Subscript 1 and 2 denotes the full-scale situation and the scaled model situation, respectively. Similarly, the frequency f_2 can be corrected to the full-scale value f_1 by

$$\frac{f_1}{f_2} = \frac{U_1}{U_2} \times \frac{D_2}{D_1} \tag{4}$$

As mentioned earlier, the running speed in the simulations is reduced to 10 m/s, but will be rescaled to 400 km/h, approximately a factor of 11.1, while the dimensions of the bogie model are also scaled down by a factor of 1/12. The distance to the receiver is kept constant. Therefore, to adjust the calculated noise during rescaling, a correction ΔSPL of 84.3 dB is incorporated. Furthermore, according to Equation (4), the frequency ratio is approximately 0.93 and is applied when scaling the frequencies.
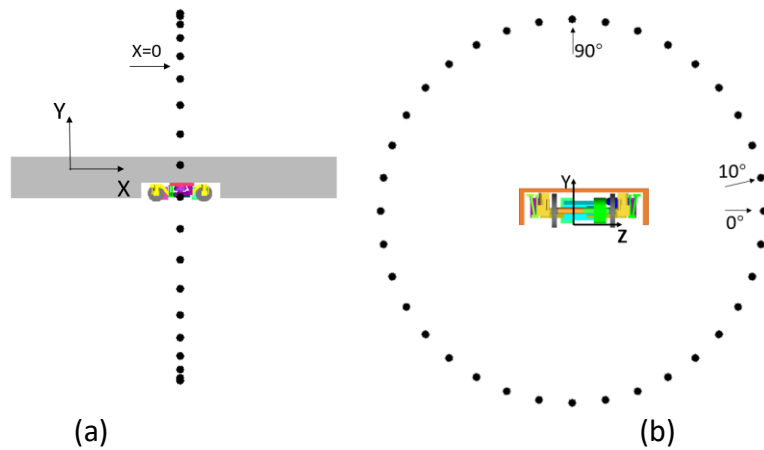

Figure 16 Sketch of the receiver locations. (a) Side view; (b) front view.

Figure 16 depicts the 36 receivers placed around the bogie. The receivers are evenly distributed with an angular interval of 10°. The distance between the receivers

and the centre of the bogie is 20 m, which is greater than the largest acoustic wavelength of interest (17.25 m at 20 Hz) and meets the requirements for the acoustic far field. For the sound propagation, free-field conditions are assumed and acoustic shielding and scattering effects are neglected.
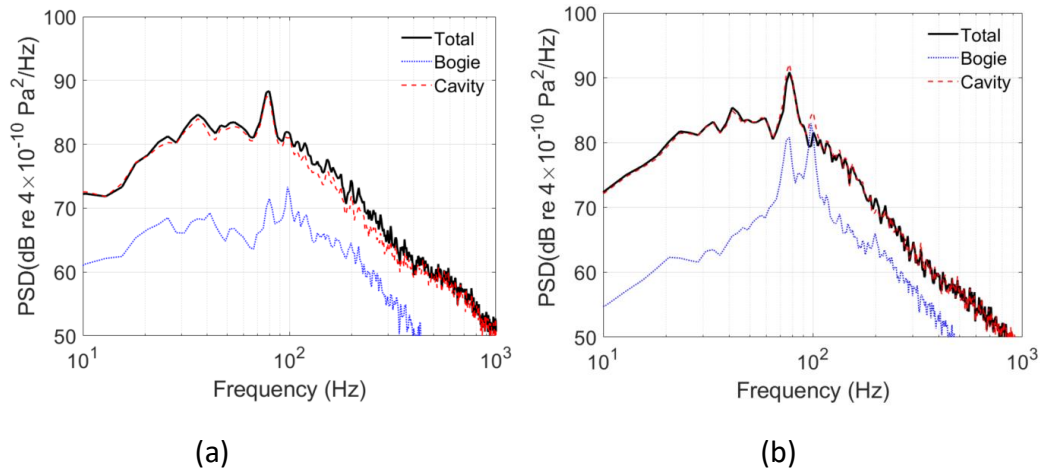

(a)   (b)

Figure 17 Noise spectra of the model at the side and top receivers, scaled to full-scale case at a distance of 20 m distance. (a) Side, 0°; (b) top, 90°.

Figure 17 illustrates the noise spectra of the cavity and bogie at the side and top receivers (at 0° and 90° as shown in Figure 16). In general, the noise produced by the bogie is significantly lower than that generated by the cavity. In addition, for both the bogie and the cavity, the noise spectra are dominated by frequencies below approximately 200 Hz, which is consistent with the findings from Lauterbach et al. [5] and Latorre Iglesias et al. [9]. Based on the above analysis, it can be inferred that the generation of the noise at low frequencies is associated with large-scale flow phenomena, such as flow circulation, flapping and flow recirculation, observed particularly at the rear section of the cavity, as displayed in Figure 8 and Figure 9. Additionally, both spectra exhibit a minor peak at 78 Hz, with a secondary peak at approximately 100 Hz in the bogie spectra. These peaks are presumed to be associated with the shear layer detached from upstream and are investigated in more detail below.

Figure 18 presents the directivity of the OASPL generated by both the bogie and the cavity under the assumption of free-field propagation. Although neglecting shielding, reflection and scattering effects, this provides an indication of the direction of sound radiation. According to Figure 18, the noise produced by the cavity exceeds that generated by the bogie by a significant margin in all directions. Yamazaki et al. [11] and

Latorre Iglesias et al. [9] also obtained this conclusion experimentally. However, in their experiments it was assumed that the flow conditions remained unaffected by the introduction of bogie components into the cavity. Moreover, in reality, the rear corners of the cavity are frequently modified to minimize drag and noise, thus reducing the cavity noise contribution compared with this simplified geometry. The OASPL of the cavity appears to be roughly omnidirectional, whereas the bogie demonstrates stronger radiation in the vertical direction.
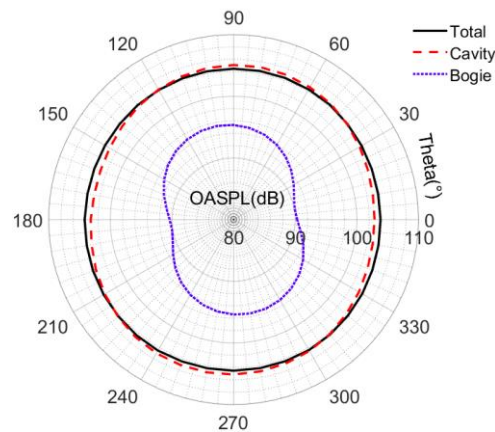
Figure 18 The far-field noise directivity of the OASPL from the model in a vertical plane, rescaled to full-scale case at a distance of 20 m.

To determine the relative contributions of different components, the bogie was partitioned into three groups: the upstream dynamic system, the downstream dynamic system, and the frame system. The dynamic systems encompass the upstream/downstream wheelsets, gearboxes, motors, and axle boxes. The frame group comprises components such as the frame, dampers, and air springs. Figure 19 shows the sound pressure spectra due to the three groups of bogie components at the side and top receivers. The noise spectra are calculated from the FW-H equation using sources on the component surfaces within the corresponding group. It is found that the noise levels from the downstream dynamic components are higher at all frequencies. This is consistent with the results given in Figure 11(a) and (b), which show the rear part of the bogie has greater values of $L_{\hat{p}}$ due to the impingement of the wake with different size of eddies from upstream components. The noise spectra of the frame components have similar shape with those of the upstream components. Two peaks are found at frequencies of 78 Hz and 100 Hz.
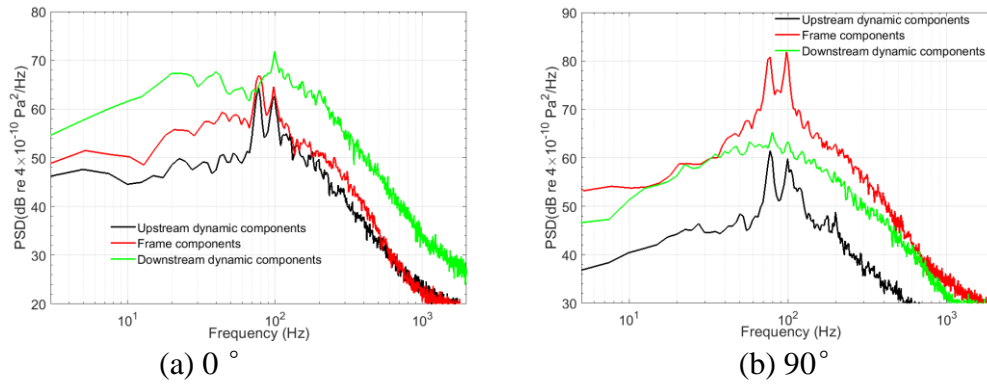
(a) 0°   (b) 90°

Figure 19 Sound pressure spectra of the bogie components

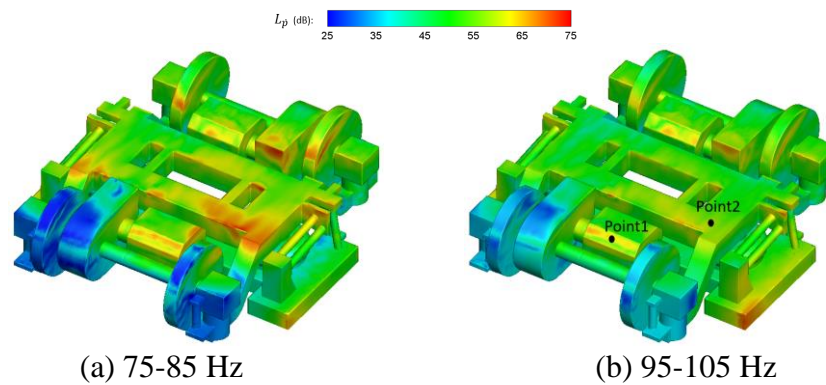(a) 75-85 Hz   (b) 95-105 Hz

Figure 20 Surface contours of the pressure rate of change dp/dt on the bogie integrated around the peak frequencies in Figure 19. (Bottom view)

To identify the flow mechanisms responsible for the peaks, Figure 20 shows the strength of pressure fluctuation integrated over frequency bands of 75-85 and 95-105 Hz by equation (1). It can be noted that strong pressure fluctuations appear in areas on which the shear layer directly impinges. Two monitors are placed within the area with strong pressure fluctuations, as indicated. Figure 21 depicts the spectra of the pressure coefficients (C_p) at these two monitors. Two peaks are also identified, and have the same frequencies as found in the noise spectra of bogie components given in Figure 19. They are related to the vortices shed periodically from upstream of the cavity rim (Lauterbach et al. [5]). These vortices are then convected downstream as the shear layer propagates with convection and breaks after impinging on the downstream components. The breakdown of these vortices is the reason why the peaks are not as significant in the noise spectra of the downstream dynamic components as they are for the upstream dynamic components.
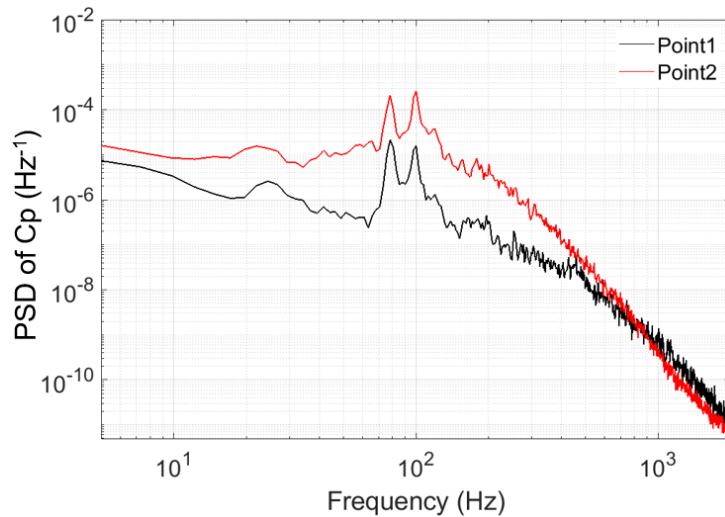
23

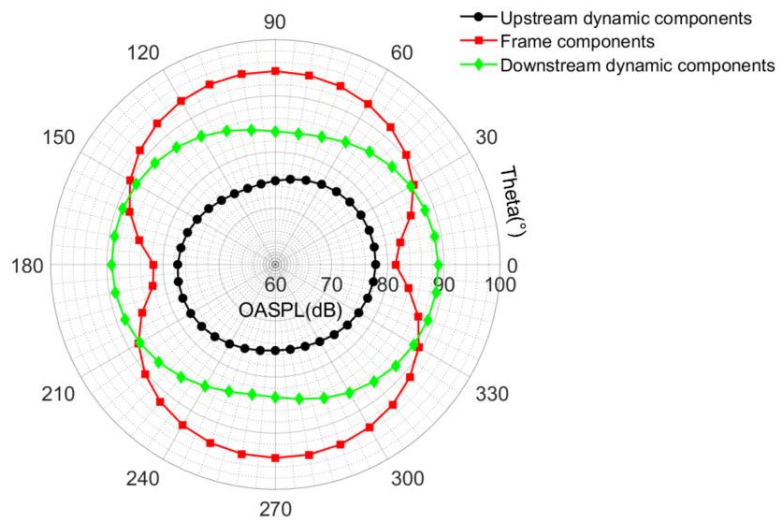Figure 21 PSD of $Cp(t)$ of Point1 and Point2 in Figure 20(b).

Figure 22 Noise directivity of the bogie components

Figure 22 shows the directivities of the noise from the bogie components. It is worth noting that the dynamic components emit greater OASPLs in the horizontal direction, while the frame components emit larger ones in the vertical direction. Therefore, for the directivity of the bogie, as shown in Figure 18, the dynamic components contribute more in the lateral direction while the frame components contribute more in the vertical direction. In addition, the directivity of the frame components is symmetric with respect to the lateral mid-plane, whereas for the dynamic components it is asymmetric due to the positions of the motors and gearboxes. Consequently, the directivity of the whole bogie, determined by both the frame components and dynamic components, is slightly oblique to the left, as shown in Figure 18.

In Figure 18, the directivity of the cavity is nearly omnidirectional, while the bogie exhibits stronger radiation in the vertical direction. This difference can be attributed to the differences in the noise source distribution on the surfaces of the bogie and the cavity. As shown in Figure 11(b), Figure 14 and Figure 15, the bottom surface of the frame components shows strong noise source covering a larger area than the lateral projected area of the downstream dynamic components, which is also covered by strong noise sources. Consequently, as shown in Figure 22, the maximum noise level of the frame components is higher in the vertical direction than that of the downstream components in the lateral direction. Thus, the noise directivity of the bogie exhibits higher values in the vertical direction. However, regarding the noise distribution at the rear part of the cavity, as shown in Figure 11(c), Figure 12 and Figure 13, the vertical and lateral areas with strong noise sources are similar. This balanced distribution results in the directivity of the cavity being close to omnidirectional.

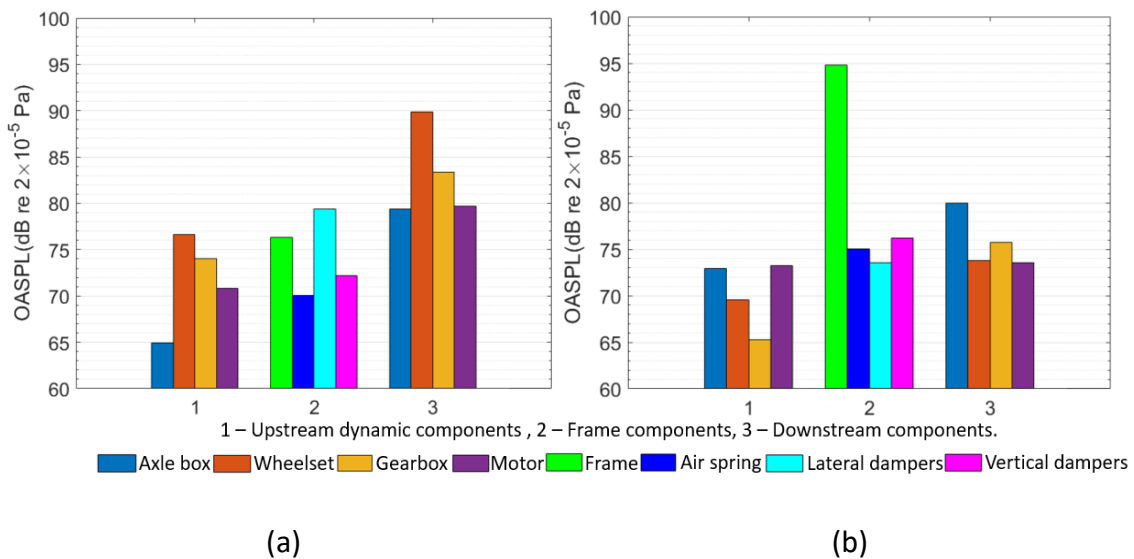(a)   (b)

Figure 23 Noise levels produced by different bogie components at side and top receivers. (a) Side, 0°; (b) top, 90°.

Figure 23 compares the OASPLs at the side and top receivers. This reveals the potential noise contributions of different bogie components: upwards to the interior of the car and sideways to the surrounding environment. As shown in Figure 23(a), the wheelsets contribute the most in the lateral direction among the various bogie components. This observation is consistent with the experimental results of Yamazaki et al. [11]. At the side receiver, their noise levels exceed those at the top receiver. As shown in Figure 11, the values of $L_{\dot{p}}$ are comparable between the wheel rim and the side

surfaces of the wheels. However, due to the larger area of the side surface, the SPL in the lateral direction is larger than that in the upward direction. Similarly, as depicted in Figure 23(b), also because bottom of the frame has a larger surface area, the SPL of the frame significantly exceeds that of the other components in the vertical direction.

5.   Conclusions

A numerical approach has been proposed to analyse the aerodynamic noise generated by a train bogie with realistic geometric features. To discretise the complex bogie model with high-quality and affordable meshes, a hybrid grid system was implemented. This system incorporates a hexahedral grid near the solid surface and a polyhedral grid throughout the remaining volume. Circular and square cylinders were utilized to validate the effectiveness of the hybrid grid concept. Subsequently, a grid sensitivity study was conducted using a half-width model, with the bogie in the model simplified to reduce the computational cost. The chosen grid parameters were then implemented to calculate the noise generated by the complete bogie model within a simplified cavity.

The aerodynamic results reveal that both the shear layer and the turbulent wake from the upstream components contribute to the aerodynamic noise from the bogie. Potential noise source regions are identified as components immersed in either the detached shear layer or the turbulent wake. This is supported by the examination of the distribution of the rate of change of pressure dp/dt. The rear section of the bogie and regions around the rear cavity corner show high noise source strengths due to the impingement of vortical shear layers and turbulent wakes from upstream components. These results offer valuable insights for future noise reduction measures. The characteristics of the far-field noise from the bogie and cavity were also calculated. It was found that the noise level produced by the cavity exceeded that of the bogie, both being dominated by frequencies below approximately 200 Hz. The low frequency noise mainly originates from the bottom surfaces of the bogie and the rear wall of the bogie cavity. These findings align with experimental studies from Latorre Iglesias et al. [9] and Yamazaki et al. [11]. It was observed that the rear components of the bogie produced higher noise levels than those at the front, a trend consistent with findings reported in the experimental study by Sawamura et al. [10].

However, it is important to note some limitations. This study focused only on the bogie, the most complex part, while simplifying the car body to a simple geometry with a cavity. A realistic car body, for which the hybrid grid method should be well adapted, is necessary to assess its impact on the aerodynamic noise.

References

1. Talotte C. Aerodynamic noise: a critical survey. Journal of Sound and Vibration. 2000;231(3):549-62.
2. Martens A, Wedemann J, Meunier N, Leclere A. High speed train noise-sound source localization at fast passing trains. Sociedad Espanola de Acoustica, SEA. 2009.
3. Nagakura K. Localization of aerodynamic noise sources of Shinkansen trains. Journal of Sound and Vibration. 2006;293(3):547-56.
4. Thompson DJ, Latorre Iglesias E, Liu X, Zhu J, Hu Z. Recent developments in the prediction and control of aerodynamic noise from high-speed trains. International Journal of Rail Transportation. 2015;3(3):119-50.
5. Lauterbach A, Ehrenfried K, Loose S, Wagner C. Microphone Array Wind Tunnel Measurements of Reynolds Number Effects in High-Speed Train Aeroacoustics. International Journal of Aeroacoustics. 2012;11(3-4):411-46.
6. Liu X, Zhang J, Thompson DJ, Latorre Iglesias E, et al. Aerodynamic noise of high-speed train pantographs: Comparisons between field measurements and an updated component-based prediction model. Applied Acoustics. 2021;175:107791.
7. Noh H-M, Choi S, Hong S, Kim S-W. Investigation of noise sources in high-speed trains. Proceedings of the Institution of Mechanical Engineers, Part F: Journal of Rail and Rapid Transit. 2014;228(3):307-22.
8. Uda T, Yamazaki N, Kitagawa T, Nagakura K, Wakabayashi Y. Estimation of Aerodynamic Bogie Noise Through Field and Wind Tunnel Tests. Noise and Vibration Mitigation for Rail Transportation Systems: Proceedings of the 12th International Workshop on Railway Noise, 12-16 September 2016, Terrigal, Australia. 139: Springer; 2018. p. 377-87.
9. Latorre Iglesias E, Thompson DJ, Smith M, Kitagawa T, Yamazaki N. Anechoic wind tunnel tests on high-speed train bogie aerodynamic noise. International Journal of Rail Transportation. 2017;5(2):87-109.

10. Sawamura Y, Uda T, Kitagawa T, Yokoyama H, Iida A. Measurement and Reduction of the Aerodynamic Bogie Noise Generated by High-Speed Trains in Terms of Wind Tunnel Testing. In: Degrande G, et al., editors. Noise and Vibration Mitigation for Rail Transportation Systems;Noise and Vibration Mitigation for Rail Transportation Systems Notes on Numerical Fluid Mechanics and Multidisciplinary Design; Cham: Springer International Publishing; 2021. p. 73-80,https://doi.org/10.1007/978-3-030-70289-2_5.

11. Yamazaki N, Uda T, Kitagawa T, Wakabayashi Y. Influence of Bogie Components on Aerodynamic Bogie Noise Generated from Shinkansen Trains. Quarterly Report of RTRI. 2019;60(3):202-7.

12. Zhang J, Wang J, Wang Q, Xiong X, Gao G. A study of the influence of bogie cut outs' angles on the aerodynamic performance of a high-speed train. Journal of Wind Engineering and Industrial Aerodynamics. 2018;175:153-68.

13. Wang J, Minelli G, Dong T, He K, Krajnović S. Impact of the bogies and cavities on the aerodynamic behaviour of a high-speed train. An IDDES study. Journal of Wind Engineering and Industrial Aerodynamics. 2020;207:104406.

14. Liang X-f, Liu H-f, Dong T-y, Yang Z-g, Tan X-m. Aerodynamic noise characteristics of high-speed train foremost bogie section. Journal of Central South University. 2020;27(6):1802-13.

15. Lan J, Han J. Research on the radiation characteristics of aerodynamic noises of a simplified bogie of the high-speed train. Journal of Vibroengineering. 2017;19(3).

16. Ali JM, Omar AA, Ali MAB, Baseair ARBM, editors. Numerical Investigation of Aerodynamic Characteristics of High Speed Train. IOP Conference Series: Materials Science and Engineering; 2017: IOP Publishing **184 :**012015.

17. Zhu C, Hemida H, Flynn D, Baker C, Liang X, Zhou D. Numerical simulation of the slipstream and aeroacoustic field around a high-speed train. Proceedings of the Institution of Mechanical Engineers, Part F: Journal of Rail and Rapid Transit. 2017;231(6):740-56.

18. Dong T, Liang X, Krajnović S, Xiong X, Zhou W. Effects of simplifying train bogies on surrounding flow and aerodynamic forces. Journal of Wind Engineering and Industrial Aerodynamics. 2019;191:170-82.

19. Guo Z, Liu T, Chen Z, Xia Y, Li W, Li L. Aerodynamic influences of bogie's geometric complexity on high-speed trains under crosswind. Journal of Wind Engineering and Industrial Aerodynamics. 2020;196:104053.

20. Zhu J, Hu Z, Thompson D. Flow simulation and aerodynamic noise prediction for a high-speed train wheelset. International Journal of Aeroacoustics. 2014;13(7-8):533-52.

21. Zhu J, Hu Z, Thompson DJ. Flow behaviour and aeroacoustic characteristics of a simplified high-speed train bogie. Proceedings of the Institution of Mechanical Engineers, Part F: Journal of Rail and Rapid Transit. 2016;230(7):1642-58.

22. Zhu J, Hu Z, Thompson D. The flow and flow-induced noise behaviour of a simplified high-speed train bogie in the cavity with and without a fairing. Proceedings of the Institution of Mechanical Engineers, Part F: Journal of Rail and Rapid Transit. 2018;232(3):759-73.

23. Zhu J, Hu Z, Thompson D. The effect of a moving ground on the flow and aerodynamic noise behaviour of a simplified high-speed train bogie. International Journal of Rail Transportation. 2017;5(2):110-25.

24. Li C, Zhu J, Hu Z, Lei Z, Zhu Y. Investigation on aerodynamic noise generated from the simplified high-speed train leading cars. International Journal of Aeroacoustics. 2022:1475472X221093701.

25. Spalart PR, Streett C. Young-person's guide to detached-eddy simulation grids. 2001:No. NAS 1.26: 211032.

26. Spalart P, Allmaras S. A one-equation turbulence model for aerodynamic flows. 30th aerospace sciences meeting and exhibit1992. p. 439.

27. Shur M, Spalart P, Strelets M, Travin A. Detached-eddy simulation of an airfoil at high angle of attack. Proceedings of the 4th International Symposium on Engineering Turbulence Modelling and Measurements; 24–26, May, 1999; Ajaccio, Corsica, France: Elsevier; 1999. p. 669-78.

28. Hefny MM, Ooka R. CFD analysis of pollutant dispersion around buildings: Effect of cell geometry. Building and Environment. 2009;44(8):1699-706.

29. Chen H, Zhou X, Feng Z, Cao S-J. Application of polyhedral meshing strategy in indoor environment simulation: Model accuracy and computing time. Indoor and Built Environment. 2022;31(3):719-31.

30. Duan R, Liu W, Xu L, Huang Y, et al. Mesh type and number for the CFD simulations of air distribution in an aircraft cabin. Numerical heat transfer, part B: fundamentals. 2015;67(6):489-506.

31. Peric M, Ferguson S. The advantage of polyhedral meshes. Dynamics. 2005;24:45.

32. Liu Y, Long Z, Liu W. A semi-empirical mesh strategy for CFD simulation of indoor airflow. Indoor and Built Environment. 2022:1420326X221089825.

33. Juretić F, Gosman A. Error analysis of the finite-volume method with respect to mesh type. Numerical heat transfer, part B: fundamentals. 2010;57(6):414-39.

34. Shaw J, Peace A. Simulating three‐dimensional aeronautical flows on mixed block‐structured/semi‐structured/unstructured meshes. International Journal for Numerical Methods in Fluids. 2002;39(3):213-46.

35. Tysell L. Hybrid grid generation for complex 3D geometries. 2010.

36. Becker K, Heitkamp K, Kügeler E. Recent progress in a hybrid-grid CFD solver for turbomachinery flows. Proceedings fifth European conference on computational fluid dynamics ECCOMAS CFD2010.

37. Spalart PR, Deck S, Shur ML, Squires KD, Strelets MK, Travin A. A New Version of Detached-eddy Simulation, Resistant to Ambiguous Grid Densities. Theoretical and Computational Fluid Dynamics. 2006;20(3):181.

38. Spalart PR. Strategies for turbulence modelling and simulations. International journal of heat and fluid flow. 2000;21(3):252-63.

39. Carley M. Turbulence and noise. Chapter 5: The generation of sound: https://people.bath.ac.uk/ensmjc/Notes/tnoise.pdf; 2011.

40. Liu X. Aerodynamic noise from components of a train pantograph and its reduction. PhD thesis, University of Southampton. 2017.

41. Liu X, Thompson DJ, Hu Z. Numerical investigation of aerodynamic noise generated by circular cylinders in cross-flow at Reynolds numbers in the upper subcritical and critical regimes. International Journal of Aeroacoustics. 2019;18(4-5):470-95.

42. Liu X, Hu Z, Thompson D, Jurdic V. Reduction of aerodynamic noise from square bars by introducing spanwise waviness. Journal of Sound and Vibration. 2018;435:323-49.

43. Schewe G. On the force fluctuations acting on a circular cylinder in crossflow from subcritical up to transcritical Reynolds numbers. Journal of Fluid Mechanics. 1983;133:265-85.

44. Norberg C. Flow around a circular cylinder: aspects of fluctuating lift. Journal of Fluids and Structures. 2001;15(3):459-69.

45. Vickery BJ. Fluctuating lift and drag on a long cylinder of square cross-section in a smooth and in a turbulent stream. Journal of Fluid Mechanics. 1966;25(3):481-94.

46. Norberg C. Flow around rectangular cylinders: Pressure forces and wake frequencies. Journal of Wind Engineering and Industrial Aerodynamics. 1993;49(1):187-96.

47. Farassat F. Derivation of Formulations 1 and 1A of Farassat. Tech Report, NASA TM-2007–214853. 2007.

48. He Y. Aerodynamic noise simulation of high-speed train bogie. PhD thesis, University of Southampton. 2023.

49. Morris SC. Shear-layer instabilities: particle image velocimetry measurements and implications for acoustics. Annual Review of Fluid Mechanics. 2011;43:529-50.

50. Curle N. The influence of solid boundaries upon aerodynamic sound. Proc R Soc Lond A. 1955;231(1187):505-14.